Optomechanics based soft artificial skin

Abhijit Chandra Roy (abhijit.ch.roy1@gmail.com)
IISc Bangalore, India https://orcid.org/0000-0002-1801-289X

Navin Kumar
IISc Bangalore, India

Shreyas B S
IISc Bangalore, India

Ananya Gupta
IISc Bangalore, India

Aloke Kumar
IISc Bangalore, India

V. Venkataraman
IISc Bangalore, India

Research Article

Keywords: Artificial electronic skin, soft robotics, contact mechanics, deformation of soft material, soft 3D printing

Posted Date: August 2nd, 2021

DOI: https://doi.org/10.21203/rs.3.rs-763714/v1

Optomechanics based soft artificial skin

Abhijit Chandra Roy*[1], Navin Kumar[1], Shreyas B S[1], Ananya Gupta[1], Aloke Kumar[2] and V. Venkataraman[1]†

1. Department of Physics, Indian Institute of Science, Bangalore, Karnataka, India-560012
2. Department of Mechanical Engineering, Indian Institute of Science, Bangalore, Karnataka, India-560012

* Corresponding author's E-mail: abhijitroy@iisc.ac.in
† Author now deceased, died on 24th Jan 2020.

Keywords: Artificial electronic skin, soft robotics, contact mechanics, deformation of soft material, soft 3D printing

Abstract

Soft artificial skin capable of sensing touch, pressure and bending similar to soft human skin is important in many modern-day applications including socially interactive robotics, modern healthcare, augmented reality, etc. However, most of the research effort on soft artificial skin are confined to the lab-scale demonstration. We have demonstrated how a fundamental understanding of the contact mechanics of soft material and a specially constructed soft optical waveguide let us develop a highly efficient, resilient, and large-area soft artificial skin for futuristic applications. The soft artificial skin capable of detect touch, load and bending shows extreme sensitivity (up to $150\ \mathrm{kPa}^{-1}$) to touch, and load, which is 750 times higher than earlier work. The soft-a-skin shows excellent long-term stability *i.e.* it shows consistent performance up to almost a year. In addition, we describe a 3D printing process capable of producing large areas, large numbers yet cost-effective soft artificial skin. We have shown the functioning of the soft-a-skin in various means.

1. Introduction

Soft artificial skin(soft-a-skin)[1][2][3][4] similar to human skin perceives various environmental stimuli by transducing them into an electrical signal through numerous methods[1][5][6][7]. Soft artificial skin in recent times has attracted many researchers due to the emergence of diversified field of science and technologies including the field of social interactive robots[8] [9] [10], internet of 'action' (IoA)[6], modern health-monitoring technologies[11][12][13] prosthetics[14][15][16] and augmented reality[17][18], etc. Despite several efforts in developing soft artificial skin, there are yet various substantial hurdles to make soft-a-skin suitable for real-life use and industrial-scale production[19]. For example, most of the reported works on soft-a-skin at least have one or the other shortcomings such as highly complex and expensive fabrication process, consume high power, low sensitivity, shows instability at long-term, high response time and short operational bandwidths essential to be addressed to qualify for practical

use and mass manufacturing[19]. Some works have already been published on flexible artificial skin based on various techniques such as piezoelectrics[20][21], coplanar-gate graphene transistors[22], resistive[9], capacitive[6][23][24], organic field effect transistor(OFET)[25][26][7][27], and piezoresistive[20][28], etc. Robert *et. al.* report artificial stretchable soft artificial skin using resilient polymer consisting of multilayered microchannel filled with conducting liquid[9]. Despite a linear and reproducible strain sensing, a significant hysteresis in pressure sensing has been observed in their sensor. Moreover, the chance of leakage of the conducting liquid from the channel during multiple use in a real-world environment could be another challenge. In addition, optical-based soft and stretchable artificial skin has also been reported[29][30]. The optical-based artificial skin reported by Zhenan *et. al.* based on a soft transparent optical waveguide, where upon deformation on the waveguide, light at the output reduces, accordingly the output is corelated to measure the touch/pressure[29]. Recently, the use of organic field effect transistors (OFETs) in soft artificial skin have been reported by some researchers [26][7][27][25]. However, most of them shows comparatively lower sensitivity as low as ~ 0.01 kPa^{-1} reported by Aung *et. al.*[27]. In addition, the long-term stability of the OFET is an issue which is well-known for quite some time in the scientific community[31]. Moreover, OFET based pressure measurement usually shows significantly high response time(1000 ms[7], 2000 ms[27]) compared to the value attained in this work (~60 ms). Resistive based large area flexible electronic skin also has been reported by many groups, e.g. Zhenan *et. al.* reported a large area resistive based electronic skin having comparable response time ($\tau_r \sim 50$ ms) with our soft-a-skin, however, the sensitivity of their e-skin (S~0.4 kPa^{-1}) is orders of magnitudes lesser than the sensitivity(30-150 kPa^{-1}) of our soft-a-skin[32]. Although, coplanar-gate graphene transistor[22] based flexible electronic skin shows attractive response time, however, the sensitivity (0.12 kPa^{-1}) and the pressure detection range(40kPa) of the e-skin is significantly less than the sensitivity (30-150 kPa^{-1}) and pressure detection range(350 kPa) our SAS. In addition, e-piezoresistive tactile e skin has also been reported by Hyuneui Lim *et. al.* where sensitive interlocking piezoresistive sensing elements are used[20].The sensitivity (0.165 kPa^{-1}), response time (200 ms) and pressure detection range (0.128-44 kPa) of the e-skin is lower than the sensitivity, response time and pressure detection range of our work. Zhong *et. al.* published interesting work on multifunctional electronic skin based on highly stretchable and conformable matrix network (SCMN)[6]. The e-skin is capable of detect strain, temperature, light intensity, presence of magnetic field and humidity and even pressure. Despite a broad spectrum of sensing capability of the soft-a-skin, the sensors on the skin relate to delicate conformable wirings, the disjoining of these delicate connections remain a challenge. Moreover, the making of the skin is multistep and extremely complex compared to the process of fabrication described in this report. In addition, we have shown our soft-a-skin's capability of detecting bend.

The above elaboration shows the soft artificial skin made from these conventional techniques comprises of shortcomings which need to be resolved for making them real-life applications. Keeping these shortcomings in mind, we have come up with an excellent idea of exploiting the understanding of fundamental contact mechanics of soft materials supported by JKR model (details in later part) and specially designed soft optical waveguide equipped with soft hemispherical lens (SHL) structure to make soft artificial skin.

Here, we have used the principle of contact mechanical interaction between a soft hemispherical structure and optical behavior of uniquely designed soft waveguide to make a resilient, flexible, large area, and fast 3D printable soft artificial skin. In addition to the promise of large area soft-a-skin, we have achieved significantly improved sensitivity (up to $150\ \mathrm{kPa}^{-1}$). The high sensitivity of the skin is the outcome of the introduction of a unique design of the soft optical waveguide and an additional soft hemispherical structure as a passive sensing node on the top of the waveguide. Also, we have found that the quality of the artificial skin can be improved by tuning the shape of the soft hemispherical structure (including the curvature (κ), height (h), conic constant (k) etc.) and mechanical property (say modulus of the material). Moreover, we have achieved a very quick response time (60 ms) of the soft artificial skin. The soft-a-skin is robust in terms of long-term stability *i.e.* the soft-a-skin shows a consistent performance of the soft-a-skin up to almost a year. In addition, we have shown our soft-a-skin's capability to detect bend in addition to the detection of touch/pressure. Also, we have demonstrated a very convenient and cost-effective process of making the soft artificial skin by involving ultrafast liquid 3D printing (specially designed for this purpose) capable of print large areas with a capacity of industry-scale production. Finally, we have demonstrated the working of the soft-a-skin by capturing live output signal from the sensor output during the application of loads on various sensing nodes. Also, the movements of fingers of a 3D virtual hand connected to the soft-a-skin are shown while applying loads on various soft-a-skin nodes. The simultaneous detection of bending and touching capability of the soft-a-skin is also demonstrated by modulating a 3D printed robotic hand using especially designed B-soft-a-skin attached to a hand glove (see videos SV4).

2. Working principle and design of soft-a-skin

The soft-a-skin (SAS) works on the principle of limited mode of light propagation through a specially designed soft optical waveguide and soft hemispherical structure. **Figure 1a** show 2D side view schematic of an axial array of soft hemispherical lens (SHL) above a soft optical waveguide (SOW) made of material with identical refractive index which are higher than air (RI, n >1) and with a slope of suitable angle. The skin is made of such an array of SHLs in both X and Y directions above

soft optical waveguide (SOW) Figure 1d (details in coming paragraphs). Each SHL works as a sensing unit which gives touch and load value at that point. We have separately made a unit of the soft-a-skin, *i.e.* soft-a-skin cell (SAS-Cell) with SHL to understand, calibrate and characterize the soft-a-skin Figure 1a-b. It consists of a soft Dove prism (SDP) type structure, LED as light source, and a phototransistor as photodetector, which is shown by the red dotted box in Figure 1a.

Figure 1a and b depict the SAS-Cell where SHL is without and with contact with SDP respectively. Clearly, with no contact as in Figure 1a, light from an LED in air medium (air RI ~1) parallel to the longitudinal axis of the prism enters one sloped side of the SDP, get total internal reflection (TIR) from the top surfaces and refract back to a detector (PT) without loss. On the other hand, in Figure 1b, a fraction of the light ray escapes from getting TIR from the top surface of the SDP where both lens and SDP are in physical contact. The contact between SHL and SDP creates a bridge of homogeneous circular area of same refractive index (RI) through which light passes and reaches to the edge of the SHL Figure 1c.

The creation of a homogeneous RI circular area due to contact can be explained through contact mechanics of elastic solids. When a convex elastic solid comes into contact with another plane elastic solid, the deformation at solid-solid contact due to the applied force and surface forces can be explained by Johnson, Kendall, and Roberts (JKR) model[33]. In the insert Figure 1c, a and R represent the radius of the contact area and hemispherical lens respectively. The relation between a and R are cited in equation 1, 2, and 3. When SHL and SDP both made of same materials, Poisson ratios are same i.e. $\nu_1 = \nu_2 = \nu \sim 0.5$, i.e. the equation (2) turned into $K = \{E/(1-\nu^2)\}$. Studies show that applied load on the lens linearly varies with cube power of the radius of the contact circle i.e. a^3 [33]. Therefore, as load increase by a unit, the area increases by πa^6, which indicates the small input load can cause sufficient opening for input light for escaping from the detection by the PT. Resulting in a very highly sensitive load sensing capability of the soft-a-skin. The detailed relation of the applied load on the SHL and intensity loss at the detector output is discussed in the result section. Figure 1c shows a 3D schematic diagram of the SAS- Cell for proper 3D visualization of the unit of the soft artificial skin.

$$a^3 = \frac{R}{K}\{P + 3\pi WR + [6\pi WRP + (3\pi WR)^2]^{0.5} \quad \text{.....(1)}$$

Where

$$\frac{1}{K} = (3/4)\left\{\frac{1-\nu_1^2}{E_1} + \frac{1-\nu_2^2}{E_2}\right\} \text{.....(2)}$$

Where a is the radius of the contact area, E is the elastic moduli, W is the work of adhesion, P is an external load, ν_1 and ν_2 are Poisson ratios of the materials, R is radius of curvature of the SHL.

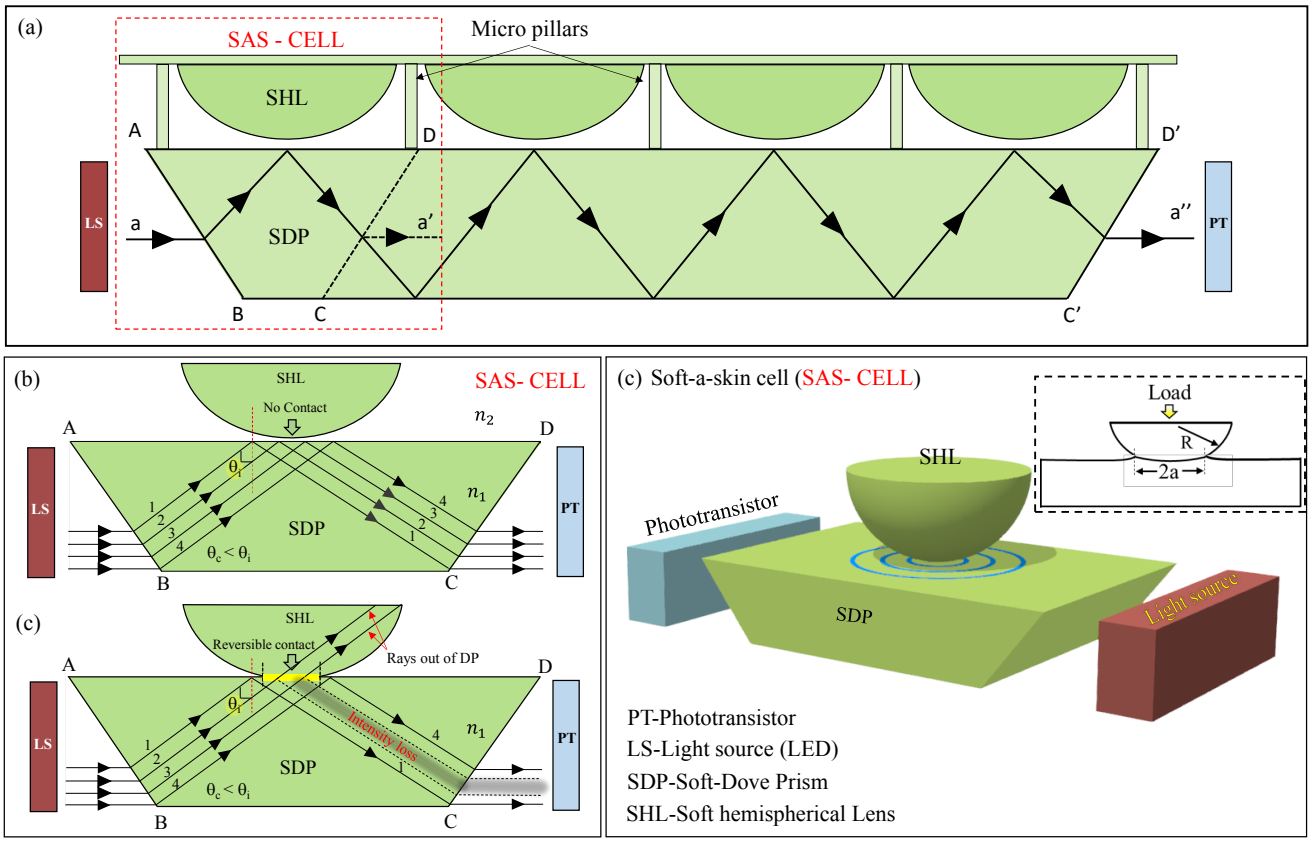

Figure 1. Schematic representation of the working principle of electronic skin (soft-a-skin). (a) 2D schematic side view and ray diagram representation of the soft artificial skin (soft-a-skin. (b) Schematic diagram of soft-a-skin unit cell (SAS-Cell), a soft hemispherical lens (SHL) before touching a Dove prism shaped soft slab. Light passes through the SAS-Cell from the light source (LS) to the photodetector (PT) without loss due to total internal reflection of light ray (TIRL). (c) SHL touches the surface of the SAS-Cell, creates a circular contact area, light otherwise totally reflected, passes through the contact area in the expanse of lowering output intensity. (d) 3D schematic representation of soft-a-skin unit cell (SAS-Cell).

3. Preparation of the soft-a-skin

The preparation of soft-a-skin is mainly divided into three broad categories namely (i) making of the array of soft hemispherical lens (SHL), (ii) making of soft rectangular optical waveguide with supporting micropillars, and (iii) 3D printed holders for sensor and the light sources. Moreover, the fabrication of the array of hemispherical lenses is conducted in two ways i.e. (a) mold-based technique and (b) custom-made liquid 3D printing-based technique. In the result and discussion section the reason of making the array of SHL in two different ways is explained.

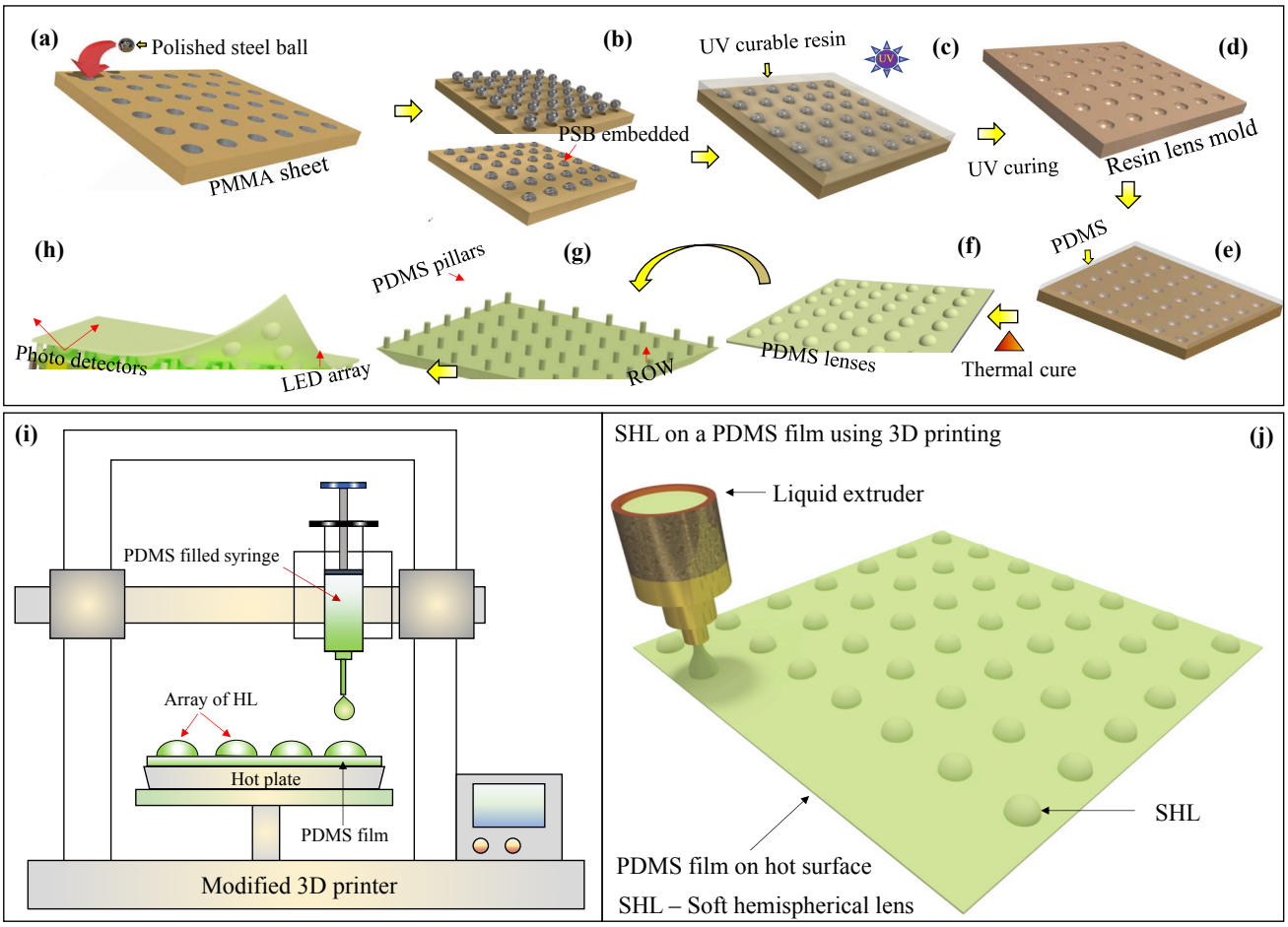

Figure 2. Mold assisted soft lithographic technique for making array of hemispherical lens structures on a PDMS film. (a) Array of through holes are made on a rectangular slab of PMMA with smooth surface, the diameter of the holes is equivalent to steel ball to be fitted on the holes. (b). Steel balls are set on the holes by silicon adhesive from the back side to make them array of hemispherical cap over the surface of the slab. (c) Making resin template for SHL. Liquid UV curable resin is poured on the array of hemispherical cap as in (b) followed by exposer of UV light for 10 minutes. (d) The cured resin attains the shape of hemispherical cap and work as a template for making array of PDMS hemispherical structures. (e) Pour the liquid PDMS on the resin mold, cure it at 60^0C for 24 hours. (f) Array of hemispherical PDMS lens extracted from resin mold after curing the PDMS. (g) Soft optical waveguide with micropillars and sloped side walls. (making of it is depicted in SI). (h) Soft artificial skin resulted from the combination of 'f', 'g' array of light sources (LED) and phototransistors (PT). (i-j) 3D printing setups for printing PDMS hemispherical lens. (for details see SI)

Figure 2a-f indicate the making of mold-based array of soft hemispherical lens structures (for details please see supplementary info Figure S1). In this step as shown in Figure 2a, an array of steel balls are attached to Poly(methyl methacrylate)(PMMA) sheet. Using this PMMA template UV curable polymer

based negative template for making the array of PDMS hemispherical structures are made, Figure 2c-d. Polydimethylsiloxane (PDMS) with a cross-linking agent (10:1 ratio) is poured on the template and cured at 60^{o}C for 12 hours, cured PDMS results a layer with array of PDMS hemispherical structures. The array of the SHL is also made by liquid 3D printing technique as shown in the Figure 3 i-j. A 3D printer is customized to print liquid PDMS on a thin PDMS film (SI, Figure S2). This 3D liquid printer helps in tailoring the array dimensions and the number of hemispherical structures in the array. The making of soft waveguide (SOW) with micropillars are conducted in a similar template-assisted soft lithography technique (for more detail see SI, Figure S1). Finally, the phototransistors (PT) are attached against each light source to the adjacent sides (two sides) by using 3D printed holders. We have used various light sources including diode LASER, LEDs and colored light sources, etc.

4. Results

We have characterized the soft-electronic-skin (SAS) by studying a single unit of the soft-a-skin cell (SAS-Cell). Figure 3a shows the schematic representation of a custom-designed instrument to calibrate the soft-a-skin cell (SAS-Cell) in terms of load and voltage. The SAS-Cell consists of a soft Dove prismatic (SDP) structure, a (collimated) light source (LED), and a photodetector (phototransistor) as shown in Figure 3a. The PDMS SHL made by using hemispherical mold (dia. varies from ~3 to 10 mm) is attached to a micro-stage for exerting load on the PDMS SDP. The displacement of the micro-stage is controlled by a computer-controlled software through a stepper motor. As discussed earlier in Figure 1b-c, when the SHL touches the SDP, an iso-refractive index contact area generates between the SHL and the SDP. As a result, light rays which otherwise experience TIR from the SDP surface, leave the SDP through the interface. We have captured optical images from the top of the SHL during the application of loads 0, 1.3, 0.53,1.17, and 2 N on the SDP through soft PDMS hemispherical lens to demonstrate the working of the soft-a-skin (see Figure 3c-g). The images in Figure 3c shows that at zero applied load, no light appears at the edge of the SHL *i.e.* light rays travel through the SDP without any loss except negligible losses due to absorption in the PDMS and reaches to the photodetector. As a result, the PT shows maximum intensity at the output. However, as applied load increases *i.e.* for loads 1.3, 0.53,1.17, and 2 N, the intensity at the edge of the SHL also increases (Figure 3d-g), and proportionally the intensity at output decreases. The formation of the contact between the SHL and the SDP is also depicted by capturing the images at various loads by replacing PT with an optical camera (Figure 3h-l). These optical images also support that with the application of increased loads, the contact area between the SDP and SHL increases. We have calibrated the applied load for SAS-Cells made of various SHLs *e.g.* PDMS, Ecoflex, and PDMS oligomer filled

hemispherical lens (OFHL) in terms of voltage shown in Figure 4a graph 1,2, and 3 respectively (SI, Figure S3 fabrication of OFHL). Although, the applied load does not directly show a linear relation with the output intensity (V_n). However, a linear relationship has been observed between the applied load through the soft hemispherical lens on the SDP and the cubic power of the output intensity (V_n^3). The relation between load F and V_n^3 can be explained through the solid-solid contact deformation model introduced by Johnson, Kendall, and Roberts in 1971 and popularly known as JKR model[34]. According to JKR model the relation among the contact radius (a), work of adhesion (W), elastic modulus (E) and applied load (F) is as cited in equation (1). Equation (1) shows the relation between a^3 and F, however, we have observed that V_n is linearly proportional to a, the radius develops due to the contact between the SHL and the SDP with R^2 value greater than 0.996 (SI, Figure S4a, measured for PDMS SHL). Therefore, we have seen an excellent linear relationship between F and V_n^3 with R^2 value greater than 0.994 up to a certain load. A previous experimental study conducted by Chaudhary *et. al.* [33] also confirms the linear relation between a^3 and F for PDMS SHL with a diameter 3 mm. PDMS SHL of diameter 3 mm shows excellent linear relation of applied load with V_n^3 up to ~1.2 N, however, beyond that load it follows nonlinearity. Within the linear region, the SAS-units with SHL diameter 3mm show sensitivity as high as ~4.1, 13, and 21.2 $kPa^{-1}$for PDMS, Ecoflex and OFHL soft hemispherical lens respectively. The results show the sensitivity of the soft-a-skin can be improved more than 3, and 5 folds when the PDMS SHL is replaced by Ecoflex and OFHL SHL respectively.

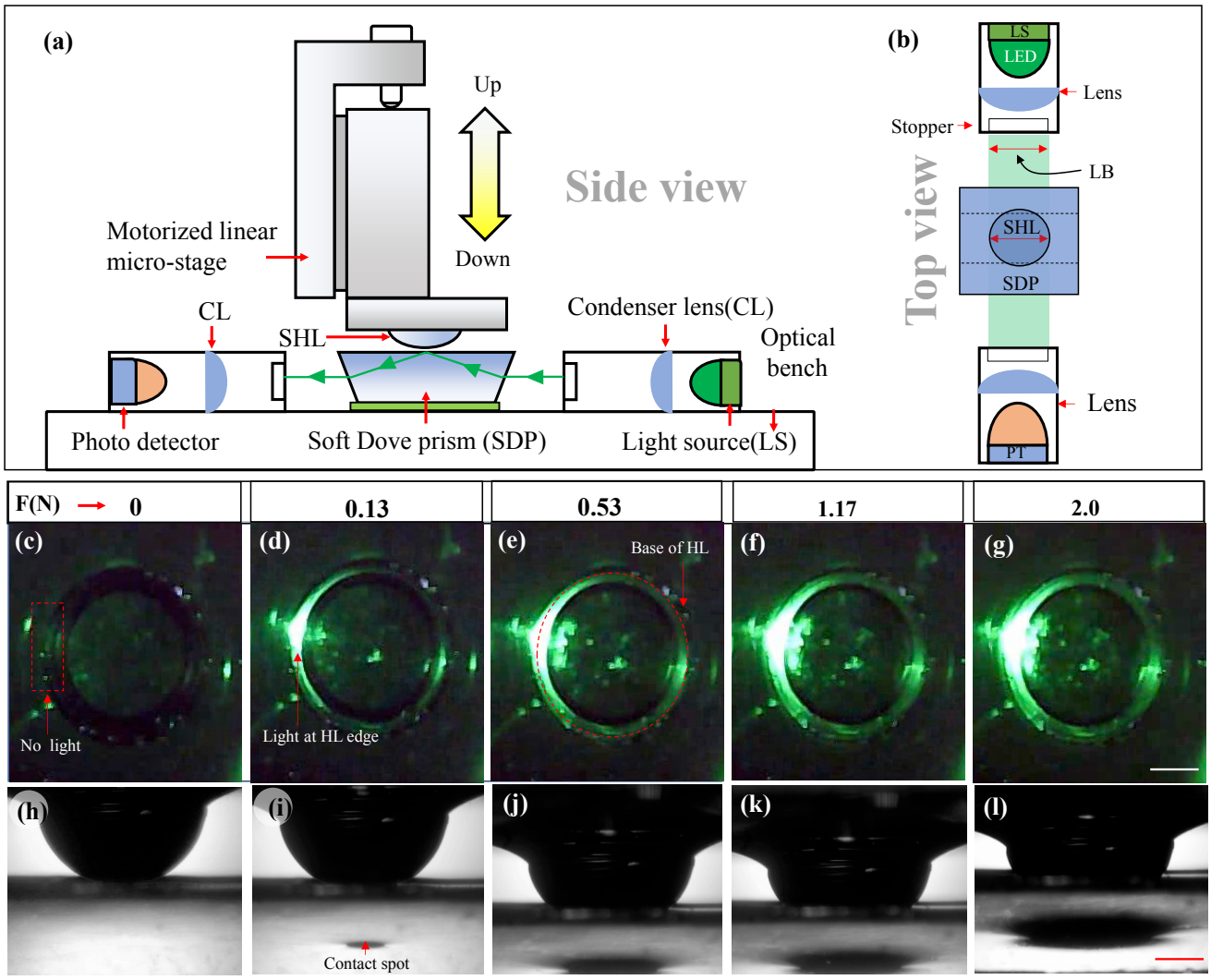

Figure 3. Characterization of the soft-a-skin. (a) Schematic diagram from the side view of a custom-made characterization tool for a soft-a-skin. (b) Top view of the of the experimental set up. (c-g) Images captured from top of the soft hemispherical lens (SHL) during the application of loads 0, 1.3, 0.53,1.17, and 2 N on the SHL. (h-l) Image captured from the side *i.e.* PT is replaced by camera and the images of both SHL and spot due to the load on SDP are captured.

Figure 4b shows the loading and unloading step loads (fixed amount of displacement ~50 µm) is exported SDP through the SHL. The graph shows no significant amount of hysteresis while loading and unloading of the probe SHL. As we mentioned earlier, the long-term stability is an issue for most of the soft-a-skin reported earlier *e.g.* OFET based soft-a-skin. Interestingly, we have observed a very stable performance of our soft-a-skin even after 10 months. We have determined the long-term stability by calibrating the soft-a-skin after more than 10 months from the first calibration of the soft-a-skin (Figure 4c). The curve with red data points indicates the initial calibration curve *i.e.* the calibration is performed before 10 months. The calibration curves with data points other than red color are captured

after 10 months. The sensitivity from those graphs shows up to 99.56% accuracy even after 10 months. Hence, in addition to the superior sensitivity of our soft-a-skin, the longer stability results give an edge over no-so-stable soft-a-skin. Insert Figure 4c (below left) shows the graphs for determining response time (τ_r) of the soft-a-skin with PDMS SHL of diameter 3 mm made by mold-based technique. The τ_r is estimated by introducing a constant load (maximum load) on the SHL and instant release of load is captured from the photodetector. Response time (τ_r) is defined as the time required to attain 90% of the stable load value from the time of the release of the load. A constant load is introduced on the 3mm diameter PDMS sensing node with a spring-enabled linear stage *i.e.* as soon as the load is released from the linear stage, the stage moves up due to spring's restoring force. The instant release of the SHL node is considered as a step load for calculating response time (τ_r) *i.e.* assuming τ_r and relaxation time is equivalent. The step load releasing event is continuously monitored by a DAQ system with a sampling rate of 1000 samples/sec *i.e.* time resolution is 1 ms. Importantly, stage is not adhered to the sensing node to avoid the role of spring's τ_r. Assuming, the τ_r of a metallic spring is significantly higher than that of the τ_r of a polymeric elastic material. The measured average τ_r for the constant pressure is ~ 63 ms. To test the robustness of the soft-a-skin, we have performed the repeatability and reproducibility test of the SAS-Cell, Figure 4d. We have chosen a step load of 24 kPa (max load at linear region) and duration of 10 sec for more than 100 times with various probe speeds namely 25, 10, 1 and 0.1 mm/sec and graphs are marked by 1, 2, 3, and 4 respectively in Figure 4d (shows 10 times repetition for better visualization). We have observed impressive repeatability of around 99.90 % (Figure 4d insert d''). However, we have observed a slightly lower reproducibility due to probe speed variation. We have achieved ~ 99.66% reproducibility compared to 99.9% repeatability. At higher probe speed, as shown in Figure 4d' the step height is slightly lesser for high-speed regime than that of low speed. This may be due to the attribution of the slight viscoelastic property (value of the loss tangent "$\tan(\delta)$" of PDMS is ~ 0.07 << 1 at 10 Hz) of PDMS[35]. The dynamic mechanical spectroscopy shows that the complex modulus ($E^* = E' + iE''$) of PDMS (PDMS: cross-linking ratio 10:1) is frequency-dependent[35] [36] (loading frequency(f_L)) i.e. the loss tangent $\tan(\delta)$ (= E''/E') is also frequency dependent (where $i^2 = -1$, E' is the storage modulus, and E'' is the loss modulus)[37].

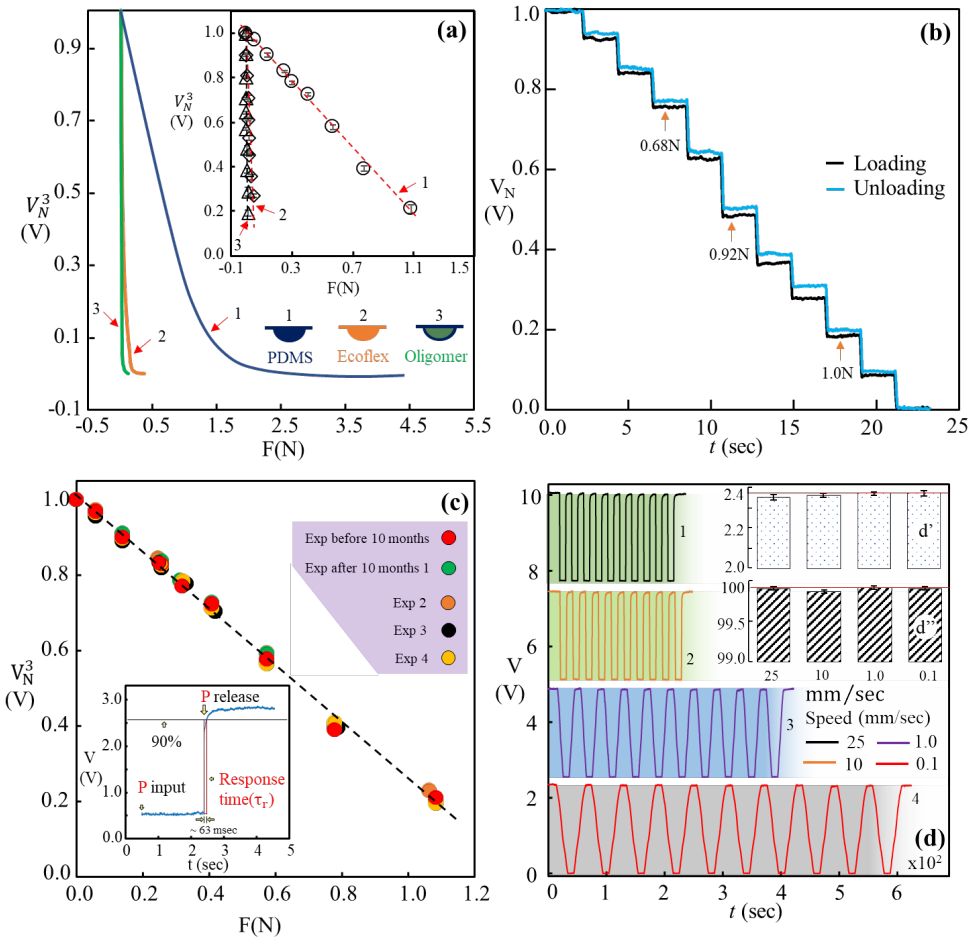

Figure 4. Characterization of the soft-a-skin unit node. (a) The plot shows the calibration between distance and load for various hemispherical lens of similar diameter 3mm. The curves 1, 2, and 3 depict SHL of 3 mm diameter made of PDMS, Ecoflex and PDMS membrane SHL filled with PDMS oligomer. (b) Step response in terms of normalized voltage at various applied loads and unloads. (c) Long term stability test in terms of soft-a-skin calibration and response time (insert image) (d) The repeatability and reproducibility of the sensor output with a wide range of speed of the soft hemispherical lens.

The storage (E′) and loss (E″)modulus represent the stored energy of the elastic portion and the dissipated energy due to the viscous portion respectively. An ideal elastic material shows zero phase-lag between stress and strain; however, it shows π/2 phase lag in case of pure viscous materials. Therefore, at high probe speed *i.e.* in the cases of 25 and 10 mm/sec, it shows a little higher value of loss tangent than at a lower probe speed. The fabrication of the array of SHL using mold-based technique has some advantages, such as, perfect array dimension, easy to fabricate, etc. However, tuning the shape and size *i.e.* various parameters such as curvature (κ), height (h), and shape i.e. conic constant(k) which includes aspherical structure (for details SI, Figure S8), require new molds which

sometime expensive to make (*e.g.* aspherical molds). Therefore, we have adopted a technique (our previous work[38]) based on rapid arresting of spreading of PDMS using quick thermally activated cross-linking and 3D liquid printing techniques to make such SHLs. Briefly, when a drop of PDMS mixed with curing agent (10:1 ratio) released on a hot ($80 - 200^oC$) smooth surface; PDMS at the interface instantly get solidified due to thermally induced cross-linking which restrict the spreading and finally it experiences complete solidification (Figure 5a). Therefore, utilizing the earlier idea we have developed a rapid 3D printing technique to make PDMS-based SHL on thin PDMS film at various substrate temperatures (T_f) with the capability of making various shapes and sizes of SHL. The design and the making of the 3D printer are explained in the material and method section (also SI, Figure S2). Figure 5 b-e shows side view optical images of the 3D printed SHLs at substrate temperatures 140^o, 160^o, 180^o and 200^oC respectively on a thin PDMS film of thickness 800μm. A comparison plot of the surface profiles of these lenses shows the distinct variety of shapes of these lenses at various temperatures (Figure 5f). The height from the base plane to the apex of the lens h is defined to find the deviation of these lenses from the perfect hemispherical nature. Figure 5h shows an excellent linear dependency of h with temperature(R^2 ~0.996). Insert bar chart of Figure 5h shows a comparison of the ratio of R/h with substrate temperature, it determines the hemispherical nature of the lens, if $R/h = 1$, the lens is a perfect hemisphere, on other hand $R/h \neq 1$ indicate condition for non-hemispherical lens. In the case of mold-based technique, the value of h and R are set equal. However, in the case of the 3D printing, as shown in insert the Figure 5h, values of R and h are not equal *i.e.* values are greater than 1, the ratio increases with the decreasing substrate temperature (Figure 5h). We have observed that although shape of the SHL changes with temperature, however at a constant amount of dispensing material, the surface area on the curved surface remains constant (Figure 5i). As temperature increases, the ratio approaches near 1 *i.e.* shape tends to become perfect hemisphere.

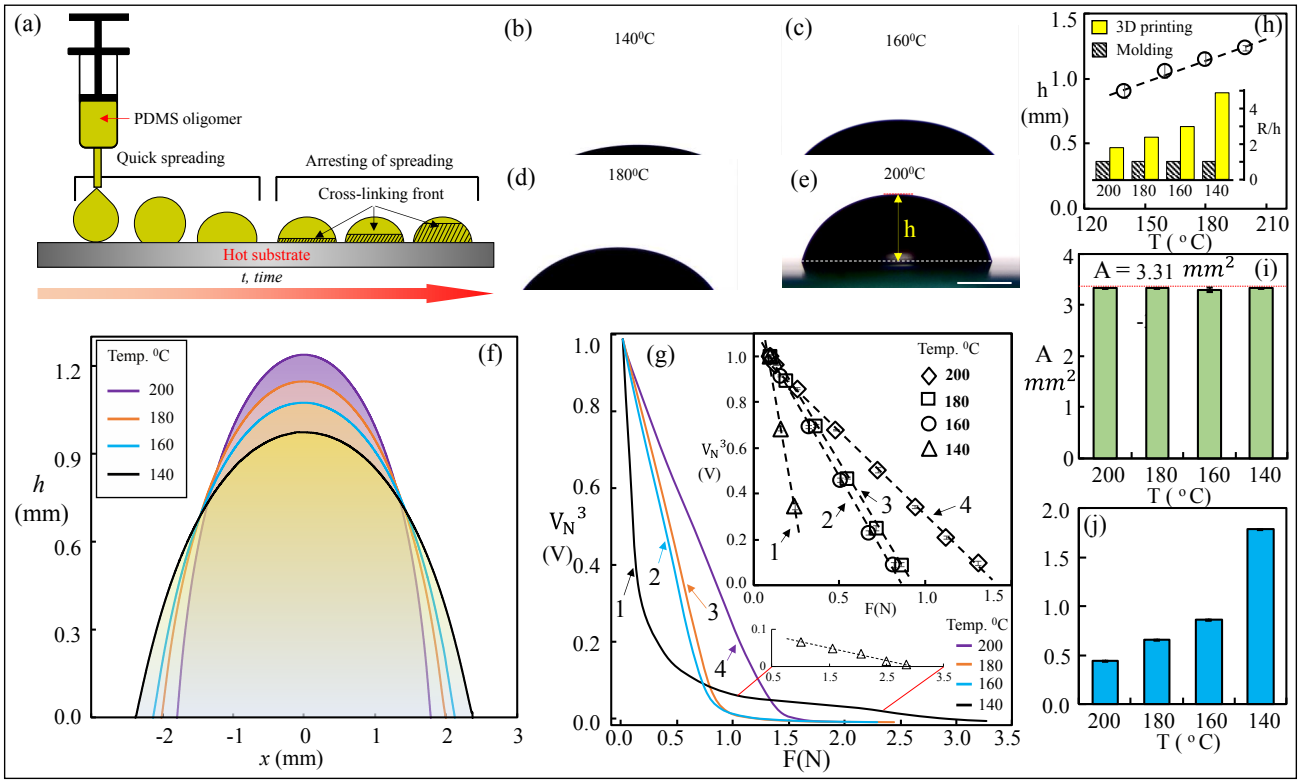

Figure 5. Characterization of 3D printable soft hemispherical lenses (SHL) on PDMS layer for making soft-a-skin. (a) Diagrammatic representation of rapid arresting of spreading of PDMS droplet due to thermal crosslinking. (b-e) Side view optical images of 3D printed lens on a thin sheet of PDMS layer at various film temperature. (f) Comparison of the surface profiles of the SHL at various film temperature (T_f). (g) The variation output intensity (V_N) at various applied load due to lenses fabricated using 3D printing at various T_f. (h) Dependence of the apex height (h) and the ratio of radius of curvature (R) to h of the lens with various T_f. (i) Bar chart of surface area of the lenses at various T_f (j) Bar chart shows variation of conic constant (k) a determining parameter of the shape of the curves due to various surface temperature.

The importance of the R/h is seen in the load calibration of these SHLs shown in Figure 5g. The R/h and the value of curvature (κ) influence the vital parameters of the soft-a-skin (SI, Figure S12, variation of contact area with R). We have observed that for the lowest value of R/h and curvature (κ) gives the height value of sensitivity (30 kPa^{-1}) and pressure detection range (350 kPa). Interestingly shape of the lenses *i.e.* value of conic constant k follows an increasing trend with surface temperature (T) of the PDMS film, Figure 5j. Our previous work shows that the conic constant k and T share a relation[38] $k \approx m/T^5$, i.e. with increasing temperature value, k decreases. In addition, the curvature (κ) associate with the temperature with a relation[38] $\kappa \approx T^2/m^{\frac{1}{3}}$ *i.e.* curvature increases with increasing temperature. Therefore, the results show as the base temperature increases, the shape of the 3D printed lenses tends

to be in a spherical shape, and as temperature decreases, it deviates more from spherical shape *i.e.* become more like an oblate spheroid. As shown in the Figure 5g, in the case of 3D printed lens also the applied load linearly varies with cubic power of intensity. The sensitivity increases with decreasing temperature of the PDMS film during fabrication. The lens fabricated at temperatures 140^{o}C shows the height sensitivity of 30 kPa^{-1} on the other hand lens made at 200^{o} C shows a sensitivity of 3.95 kPa^{-1} which is almost same as the sensitivity of the lens made by mold-based technique ($4.1kPa^{-1}$) of radius 3 mm. Also, these two lenses (3mm mold based and 200^{o} C 3D printed) show similar range of load detection 330 kPa. However, as described in earlier section (Figure 4a) in case of mold-based technique, the sensitivity of oligomer lens shows more than five folds increase in sensitivity of the solid SHLs. Therefore, lens of similar structured as 3D printed at140^{o}C filled with oligomer; the sensitivity value improves to 150 kPa^{-1}.

5. Soft-a-skin in practice

To demonstrate the working of the soft-a-skin, we have made a highly sensitive soft-a-skin using diode LASER as a light source and Ecoflex as top SHL structure. The sensing capability of the soft-a-skin with sensing node is demonstrated by capturing the output signal while exerting load at various nodes of the soft-a-skin (Figure 6a-b, a video SV1). Figure 6a shows the arrangement of light sources (Ln, n=1,2,…5) and phototransistors(Dn, n=1,2,…5). The red dots in Figure 6a represent the points on the soft-a-skin where manual physical touches/loads are applied, and the corresponding output voltage drops due to that are shown in Figure 6b. These two figures namely Figure 6a-b (also video SV1) clearly show that each touch gives a voltage drop up to about 4.5V at two particular detectors corresponding to each touchpoint *e.g.* touch T1 activates the detectors D1 and D6, T2 activates the detectors D1 and D7 and so on. In addition, a virtual 3D human hand (VH) is made using computer aided design (CAD) and the five fingers of it are connected to five detectors (PT) of soft-a-skin namely D8, D3, D9, D7 and D1 corresponding to thumb, index finger (IF), middle finger (MF), ring finger (RF) and little finger (LF) respectively. (Figure 6c-j and video SV2). Figure 6CG indicates the controlling of the index finger (IF) by touching through the sensor nodesT7 and T8 associated with light source L8 and detector D3(SI, video SV2). Since the node T9 in Figure 6 DH is common to the index and middle finger (MF), hence both fingers are controlled by applying load at T9 (SI, SV2).

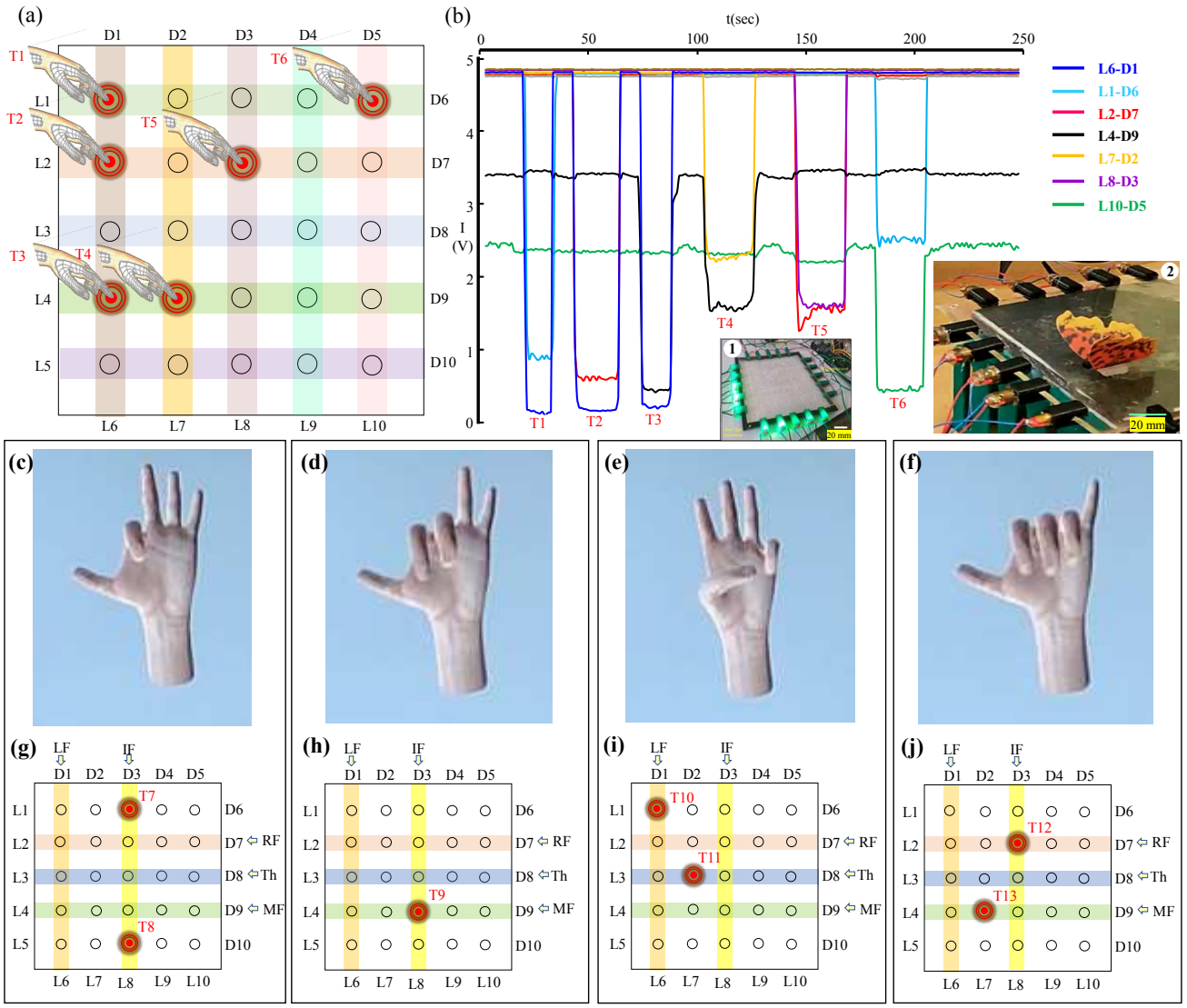

Figure 6. The visualization of the sensing capability of the soft-a-skin. (a) Diagrammatic representation of the soft-a-skin with the array of sensing nodes and their positions, light source, and the photo detectors. (b) Schematic representation of pressure perturbation created at the soft-a-skin node by a fingertip (see videos SI). (Fingers are connected to various sensors e.g., little finger (LF) to detector D1, ring finger (RF) to detector D7 and so on. Insert (b,1) optical image of a sensing node soft-a-skin made of PDMS SHLs and LEDs as light sources. Insert (b,2) demonstration of the PDMS soft-a-skin without SHLs and diodes LASERs as light sources and verify of the presence of butterfly on the soft-a-skin without SHLs. (c-f) Images of virtual hand posture result from the pressure exerted by the finger at various position represented as in the schematics(g-j) respectively.

Even we have shown controlling of two and three fingers by simultaneously applying load at two different soft-a-skin nodes. The application of simultaneous loads at node T10 and T11 activate thumb (Th) and little finger (LF), both the points are individually connected to the Th and LF. Similarly, three

fingers namely IF, MF and RF are activated by applying load on T12 and T13. The applied load at T12 activate the IF and RF and load at T13 activate the middle finger (MF). Also, to demonstrate the ultra-sensitivity of the soft-a-skin, the effect of a gentle touch of a model butterfly is shown (insert Figure 6b, video SV3). For doing that, we have removed the upper layer *i.e.* array of SHLs and a model butterfly (wt. 0.6 gm, load ~ 15 Pa) attached on a soft Ecoflex membrane is placed on the active area of the SOW which is connected to the virtual hand. Video **SV2** shows how the finger (MF) of the virtual hand experience activation and deactivation when the butterfly is attached and detached from the SOW respectively.

6. Dual sensing capability of the soft-a-skin

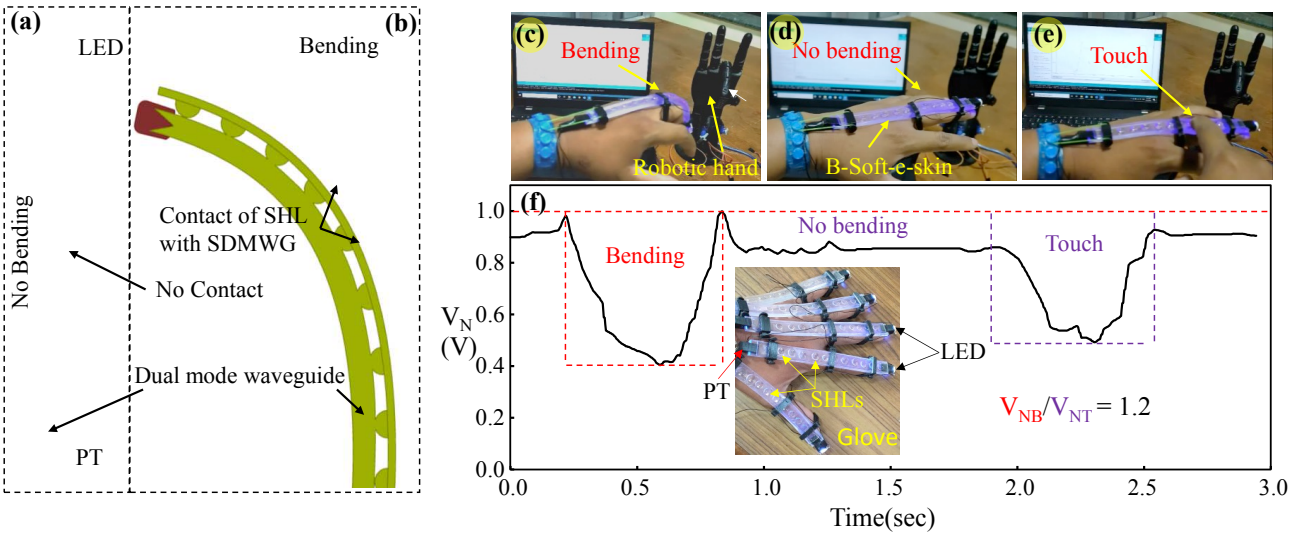

Figure 7. Bending with touch detection capability demonstration of the soft-a-skin(B-soft-a-skin). (a-b) Schematic diagram of B-soft-a-skin in normal position and bending positions respectively. (c-e) Images of finger flexing detection with the B-soft-a-skin, at bending, normal and with touch respectively. (f) B-soft-a-skin output signal for bending, normal and touch of the B-soft-a-skin. (see Video SV4)

Here in Figure 7, we demonstrate the capability of the soft-a-skin's bending and touch detection *i.e.* the capability of detecting bending and touch of a finger with a 3d printed glove. As mentioned earlier in SI, Figure S6, the importance of dual mode waveguide structure when comes to bending detection of the soft-a-skin, here in Figure 7 we have used the dual mode waveguide structure to make the soft-a-skin, we named it B-soft-a-skin. B-Soft-a-skin contain one row of SHLs above a dual mode waveguide, see schematic Figure 7 a-b. As shown in Figure 7b, because of bending, SHLs touches the dual mode waveguide structure and causes reduction of output light intensity. B-soft-a-skin which is connected to a hand glove (Figure 7 c-f, insert)) made by 3D printing and wirelessly connected to a 3D printed

robotic hand (see videoV4). Figure 7 c-e depicts the still images of the bending, normal position and touching of the B-soft-a-skin attached to a finger respectively. The corresponding skin output signal is shown Figure 7f. The bending signal of the B-soft-a-skin is ~1.2 times prominent than the touch signal. This signal amplitude differences arises as in case of bending, more than one sensing involve which contribute the output, on the other hand, touch associated with only single sensing node. Figure 7f insert figure shows the complete glove to control all the finger of the hand using the B-soft-a-skin. This experiment promises the greater adaptability and possibility of this technology for the numerous applications specially in various robotics field.

7. Discussions

The results show that the shape *i.e.* the curvature (κ), height (h), conic constant (k) of the hemispherical structure above the soft optical waveguide plays an important role in determining the sensitivity (S) and the pressure detection range of the soft-a-skin. The modulus of the soft hemispherical lens (considering other parameters constant) is also a very important parameter in determining the sensitivity and pressure detection range of the soft-a-skin. Another important finding from this work reveals that the design of the waveguide plays an important role in terms of detection of the bending as well as the spatial resolution of the soft-a-skin. We have shown that the sensitivity of the soft-a-skin made of Ecoflex (Ecoflex-00-30) SHL with mold-based technique of modulus ~ 0.07MPa is 3 times higher than ~ soft-a-skin made of PDMS SHL (PDMS: Crosslinking ratio;10:1) with modulus ~ 2MP. Further, when we use SHL made of oligomer filled hemispherical lens (OFHL, membrane thickness ~20 μm) a fivefold increment of sensitivity of the soft-a-skin has been observed, however with a compensation of pressure detection range *i.e.* pressure detection range reduce from 350 kPa to 26 kPa. In case of 3D printed SHL, we have achieved sensitivity of 30kPa^{-1}, which in case of oligomer filled SHL will leads to the maximum sensitivity 150kPa^{-1} with limit of detection (LoD) ~0.056 kPa(see SI for LoD, Figure S7). In real-world applications, the sensor with ultra-high sensitivity at lower load regime and low sensitivity at higher load is desirable. In this regards the reported soft-a-skin with 3D printed SLS shows ultra-high sensitivity 30-150kPa^{-1} at lower load < 5.3 kPa and a sensitivity of 6 kPa^{-1} at load > 5.3 kPa (Figure 5g, curve 1). The sensitivity result indicates that if we reduce the modulus of the material of SHL the sensitivity increases, however the pressure detection range reduces. To maintain a balance between the sensitivity and pressure detection range, we have proposed an idea of hybrid SHL made of two or more types of materials with decreasing modulus (SI, Figure S12, insert). The design of SOW is important not only in determining the sensitivity and pressure detection range but also the spatial density of the sensor nodes and the bendability of the soft-a-skin. We have shown

that a very high spatial resolution of SHLs and capability of bending of the soft-a-skin can easily be achieved by following the strategy discussed in (SI, Figure S6, & Figure 1). In addition, another way to resolve this issue would be to use machine learning algorithm (MLA) to find the position of the sensing node without considering the signal interference among the detectors. We have demonstrated in case of LASER light, condenser lenses are not required (videos SV1, SV2, SV3), However, in case of B-soft-a-skin we used LED due to the dual mode waveguide structure. We have observed that if the soft-a-skin is transparent stray light may affect the performance of the soft-a-skin depending upon the presence of environmental/stray light. Therefore, to overcome such problem, we have shown a way to make complete flexible opaque top membrane to obstruct the stray light (SI, Figure S11). Another important attractive prospect of our soft-a-skin is that the use of SHLs as passive sensing elements rather than using electrically connecting active/passive elements[6][25][27] which is usually vulnerable to undergo disjoints. Hence, the use of the passive soft SHL gives the freedom of stretching the soft-a-skin up to till the material fails. If we consider the overall fabrication process of the soft-a-skin, both the mold-based technique and 3D printing technique have their own advantages and limitations; however, the 3D printing technique gives more freedom in tuning parameters of SHLs and by that fine-tune of soft-a-skin within a size limit of SHL and also cost-effective compared to making new molds. A comparison table and bar chat diagram are cited in the supplementary information section for better visualization of our soft-a-skins superiority among other reported works (Table S1, Figure S13). One important issue with this present soft-a-skin is to maintain the position of the light source and photodetector unaltered after multiple use by using 3D printed external holders. However, this issue can be addressed by introducing organic light emitting diode (OLEDs) and organic photodetectors attached directly to the soft skin rather than attaching 3D printed holders.

8. Conclusion

In conclusion, many previous works have been reported on soft-a-skin by various conventional methods, however, most of them partially satisfy the criteria to be a complete realistically useable invention for real-world use. For example, although many previously reported soft-a-skins show satisfactory sensitivity but show prolonged response time and instability in long term use, etc. On the contrary, this work focuses on the realization of a practical, robust, suitable for industrial-scale production and easily scalable (3D printable) large-area soft artificial skin without compromising quality *i.e.* highly sensitive (750 times more sensitive), quick response time, bendability, stretchability etc. This reliable soft artificial skin is the outcome of the amalgamation of contact mechanical property and the optical behavior of soft materials by the use of a specially designed soft optical waveguide and

soft hemispherical structure as a sensing node. In addition, we have achieved significantly improved *i.e.* possible to attain sensitivity as high as 150 kPa^{-1} with a quick response of 63ms. The multifold increase in sensitivity is the outcome of a special design of the soft optical waveguide, and the unique aspherical shape of the soft hemispherical structures and their material property *e.g.* elastic modulus of the material. Moreover, we have observed the consistent performance of the soft-a-skin up to almost a year, an indication of better reliability of the soft-a-skin. Also, we have demonstrated a very convenient and cost-effective process of making the soft artificial skin by involving ultrafast liquid 3D printing technique (specially designed for this purpose) capable of printing large area with an ability of mass production. Interestingly, the use of SHL as a passive sensing node gives the freedom of stretching the soft-a-skin up to the limit of its material without bothering about the disjoints among the sensing nodes. Finally, we have demonstrated the working of the soft-a-skin by capturing live output signal from the sensor output during the application of loads on various sensing nodes. Also, the movements of fingers of a 3D virtual hand and a 3D printed robotic hand connect to the soft-a-skin and are shown while applying loads and bending on various soft-a-skin nodes.

9. Materials and Methods

Materials

For making the soft optical waveguide we have used Polydimethylsiloxane, PDMS (Dow corning, USA). We have used Ecoflex (Smooth-on.com) for making soft hemispherical structures and thin membranes for holding them. Activated carbon (Sigma Aldrich) is used to make opaque soft membranes to get rid of stray lights. Laser light sources and surface mounted light emitting diode (SMLEDs) are used as light source which are purchased from local electronics shop. Phototransistor (L14G2) is used as light detector.

Methods

Detail methods is explained in section " Preparation of the soft-a-skin" and further in the supplementary information Figure 1S.

Acknowledgement

The authors would like to acknowledge Dr. Sima Umrao, Dr. Veerabhadrarao Kaliginedi, Mr. K. N. Srinivasa Bhaskar for their valuable input. The authors would also like to acknowledge the Department of Science and Technology, DST, India, for providing funds for the completion of the project. Finally, the authors thank the Department of Physics, IISc Bangalore, India, for providing the laboratory space for conducting the experiments.

Funding agencies

Department of Science and Technology, DST, India.

References

[1] J. Kang, D. Son, G. J. N. Wang, Y. Liu, J. Lopez, Y. Kim, J. Y. Oh, T. Katsumata, J. Mun, Y. Lee, L. Jin, J. B. H. Tok, Z. Bao, *Adv. Mater.* **2018**, *30*, 1.

[2] X. Pu, M. Liu, X. Chen, J. Sun, C. Du, Y. Zhang, J. Zhai, W. Hu, Z. L. Wang, *Sci. Adv.* **2017**, *3*, 1.

[3] E. J. Markvicka, R. Tutika, M. D. Bartlett, C. Majidi, *Adv. Funct. Mater.* **2019**, *29*, 1.

[4] A. J. Bandodkar, J. M. You, N. H. Kim, Y. Gu, R. Kumar, A. M. V. Mohan, J. Kurniawan, S. Imani, T. Nakagawa, B. Parish, M. Parthasarathy, P. P. Mercier, S. Xu, J. Wang, *Energy Environ. Sci.* **2017**, *10*, 1581.

[5] C. To, T. L. Hellebrekers, Y. L. Park, *IEEE Int. Conf. Intell. Robot. Syst.* **2015**, *2015-Decem*, 5898.

[6] Q. Hua, J. Sun, H. Liu, R. Bao, R. Yu, J. Zhai, C. Pan, Z. L. Wang, *Nat. Commun.* **2018**, *9*, 1.

[7] S. C. B. Mannsfeld, B. C. K. Tee, R. M. Stoltenberg, C. V. H. H. Chen, S. Barman, B. V. O. Muir, A. N. Sokolov, C. Reese, Z. Bao, *Nat. Mater.* **2010**, *9*, 859.

[8] R. S. Dahiya, G. Metta, M. Valle, G. Sandini, *IEEE Trans. Robot.* **2010**, *26*, 1.

[9] Y. L. Park, B. R. Chen, R. J. Wood, *IEEE Sens. J.* **2012**, *12*, 2711.

[10] D. Silvera-Tawil, D. Rye, M. Velonaki, *Rob. Auton. Syst.* **2015**, *63*, 230.

[11] H. Keum, M. Mccormick, P. Liu, Y. Zhang, F. G. Omenetto, **2011**, *333*.

[12] C. Pang, J. H. Koo, A. Nguyen, J. M. Caves, M. G. Kim, A. Chortos, K. Kim, P. J. Wang, J. B. H. Tok, Z. Bao, *Adv. Mater.* **2015**, *27*, 634.

[13] A. Chortos, Z. Bao, *Mater. Today* **2014**, *17*, 321.

[14] A. Chortos, J. Liu, Z. Bao, *Nat. Mater.* **2016**, *15*, 937.

[15] J. Kim, M. Lee, H. J. Shim, R. Ghaffari, H. R. Cho, D. Son, Y. H. Jung, M. Soh, C. Choi, S. Jung, K. Chu, D. Jeon, S. T. Lee, J. H. Kim, S. H. Choi, T. Hyeon, D. H. Kim, *Nat. Commun.* **2014**, *5*, DOI 10.1038/ncomms6747.

[16] A. P. Gerratt, H. O. Michaud, S. P. Lacour, *Adv. Funct. Mater.* **2015**, *25*, 2287.

[17] H. Kajimoto, N. Kawakami, S. Tachi, M. Inami, *IEEE Comput. Graph. Appl.* **2004**, *24*, 36.

[18] X. Liu, K. Vega, P. Maes, J. A. Paradiso, *ACM Int. Conf. Proceeding Ser.* **2016**, *25-27-Febr*, DOI 10.1145/2875194.2875248.

[19] N. Yogeswaran, W. Dang, W. T. Navaraj, D. Shakthivel, S. Khan, E. O. Polat, S. Gupta, H. Heidari, M. Kaboli, L. Lorenzelli, G. Cheng, R. Dahiya, *Adv. Robot.* **2015**, *29*, 1359.

[20] Y. Jung, D. G. Lee, J. Park, H. Ko, H. Lim, *Sensors (Switzerland)* **2015**, *15*, 25463.

[21] I. Lee, H. J. Sung, *Exp. Fluids* **1999**, *26*, 27.

[22] Q. Sun, D. H. Kim, S. S. Park, N. Y. Lee, Y. Zhang, J. H. Lee, K. Cho, J. H. Cho, *Adv. Mater.* **2014**, *26*, 4735.

[23] D. P. J. Cotton, I. M. Graz, S. P. Lacour, *IEEE Sens. J.* **2009**, *9*, 2008.

[24] P. Cataldi, S. Dussoni, L. Ceseracciu, M. Maggiali, L. Natale, G. Metta, A. Athanassiou, I. S. Bayer, *Adv. Sci.* **2018**, *5*, DOI 10.1002/advs.201700587.

[25] T. Someya, T. Sekitani, S. Iba, Y. Kato, H. Kawaguchi, T. Sakurai, *Proc. Natl. Acad. Sci. U. S. A.* **2004**, *101*, 9966.

[26] T. Someya, Y. Kato, T. Sekitani, S. Iba, Y. Noguchi, Y. Murase, H. Kawaguchi, T. Sakurai, *Proc. Natl. Acad. Sci. U. S. A.* **2005**, *102*, 12321.

[27] A. K. K. Kyaw, H. H. C. Loh, F. Yan, J. Xu, *J. Mater. Chem. C* **2017**, *5*, 12039.

[28] X. Xiao, L. Yuan, J. Zhong, T. Ding, Y. Liu, Z. Cai, Y. Rong, H. Han, J. Zhou, Z. L. Wang, *Adv. Mater.* **2011**, *23*, 5440.

[29] M. Ramuz, B. C. K. Tee, J. B. H. Tok, Z. Bao, *Adv. Mater.* **2012**, *24*, 3223.

[30] A. Levi, M. Piovanelli, S. Furlan, B. Mazzolai, L. Beccai, *Sensors (Switzerland)* **2013**, *13*, 6578.

[31] P. A. Bobbert, A. Sharma, S. G. J. Mathijssen, M. Kemerink, D. M. De Leeuw, *Adv. Mater.* **2012**, *24*, 1146.

[32] L. Pan, A. Chortos, G. Yu, Y. Wang, S. Isaacson, R. Allen, Y. Shi, R. Dauskardt, Z. Bao, *Nat. Commun.* **2014**, *5*, DOI 10.1038/ncomms4002.

[33] M. K. Chaudhury, G. M. Whitesides, *Langmuir* **1991**, *7*, 1013.

[34] Jo, and A. D. R. nson, L.L., K.Kendall, *Proc. R. Soc. London. A. Math. Phys. Sci.* **1971**, *324*, 301.

[35] C. L. Wu, H. C. Lin, J. S. Hsu, M. C. Yip, W. Fang, *Thin Solid Films* **2009**, *517*, 4895.

[36] E. Rubino, T. Ioppolo, *J. Polym. Sci. Part B Polym. Phys.* **2016**, *54*, 747.

[37] F. Chambon, H. H. Winter, *J. Rheol. (N. Y. N. Y).* **1987**, *31*, 683.

[38] A. C. Roy, M. Yadav, E. P. Arul, A. Khanna, A. Ghatak, *Langmuir* **2016**, *32*, DOI 10.1021/acs.langmuir.5b04631.

Figures

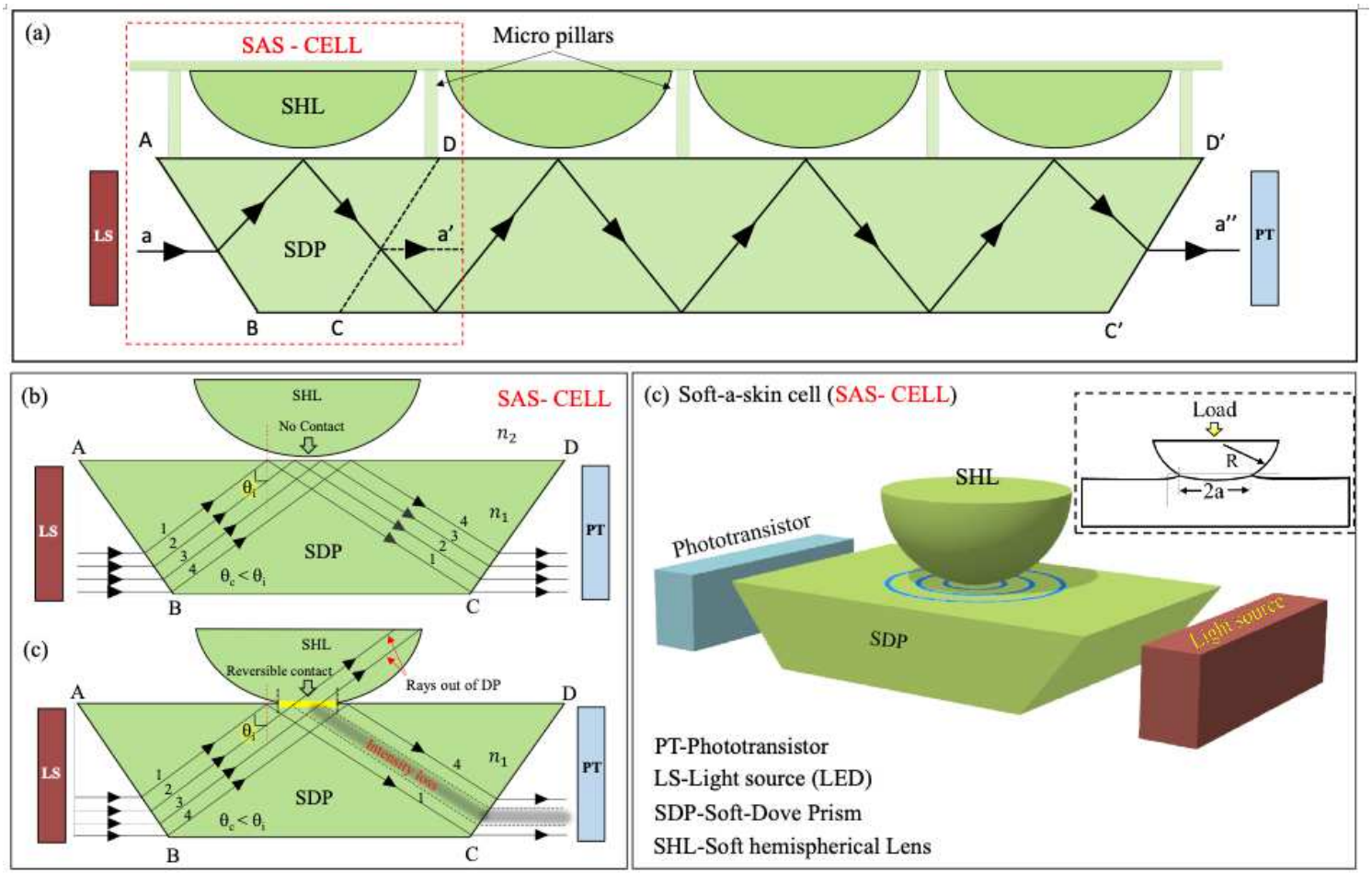

Figure 1

Schematic representation of the working principle of electronic skin (soft-a-skin). (a) 2D schematic side view and ray diagram representation of the soft artificial skin (soft-a-skin. (b) Schematic diagram of soft-a-skin unit cell (SAS-Cell), a soft hemispherical lens (SHL) before touching a Dove prism shaped soft slab. Light passes through the SAS-Cell from the light source (LS) to the photodetector (PT) without loss due to total internal reflection of light ray (TIRL). (c) SHL touches the surface of the SAS-Cell, creates a circular contact area, light otherwise totally reflected, passes through the contact area in the expanse of lowering output intensity. (d) 3D schematic representation of soft-a-skin unit cell (SAS-Cell).

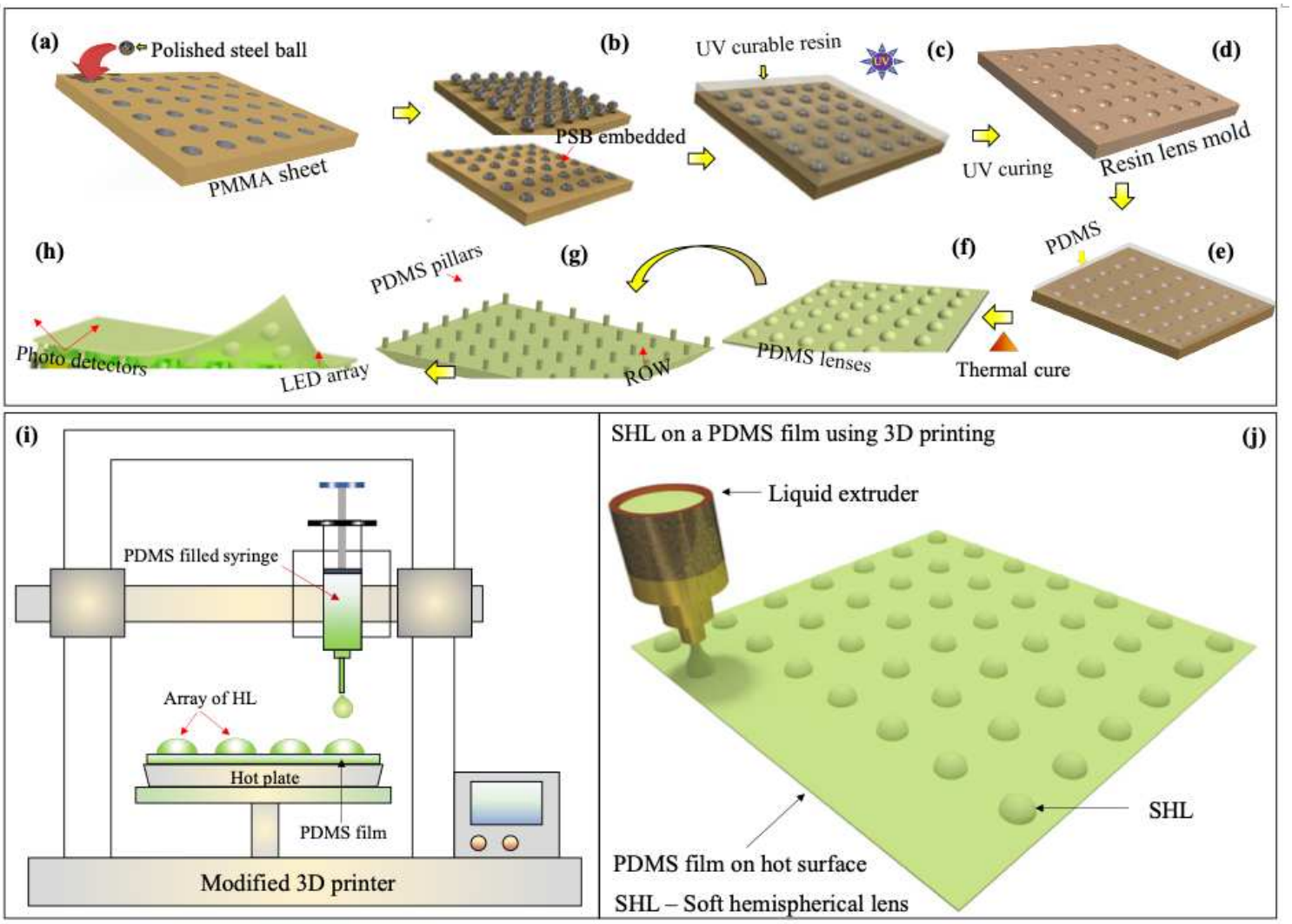

Figure 2

Mold assisted soft lithographic technique for making array of hemispherical lens structures on a PDMS film. (a) Array of through holes are made on a rectangular slab of PMMA with smooth surface, the diameter of the holes is equivalent to steel ball to be fitted on the holes. (b). Steel balls are set on the holes by silicon adhesive from the back side to make them array of hemispherical cap over the surface of the slab. (c) Making resin template for SHL. Liquid UV curable resin is poured on the array of hemispherical cap as in (b) followed by exposer of UV light for 10 minutes. (d) The cured resin attains the shape of hemispherical cap and work as a template for making array of PDMS hemispherical structures. (e) Pour the liquid PDMS on the resin mold, cure it at 60^0C for 24 hours. (f) Array of hemispherical PDMS lens extracted from resin mold after curing the PDMS. (g) Soft optical waveguide with micropillars and sloped side walls. (making of it is depicted in SI). (h) Soft artificial skin resulted from the combination of ‘f’, ‘g’ array of light sources (LED) and phototransistors (PT). (i-j) 3D printing setups for printing PDMS hemispherical lens. (for details see SI)

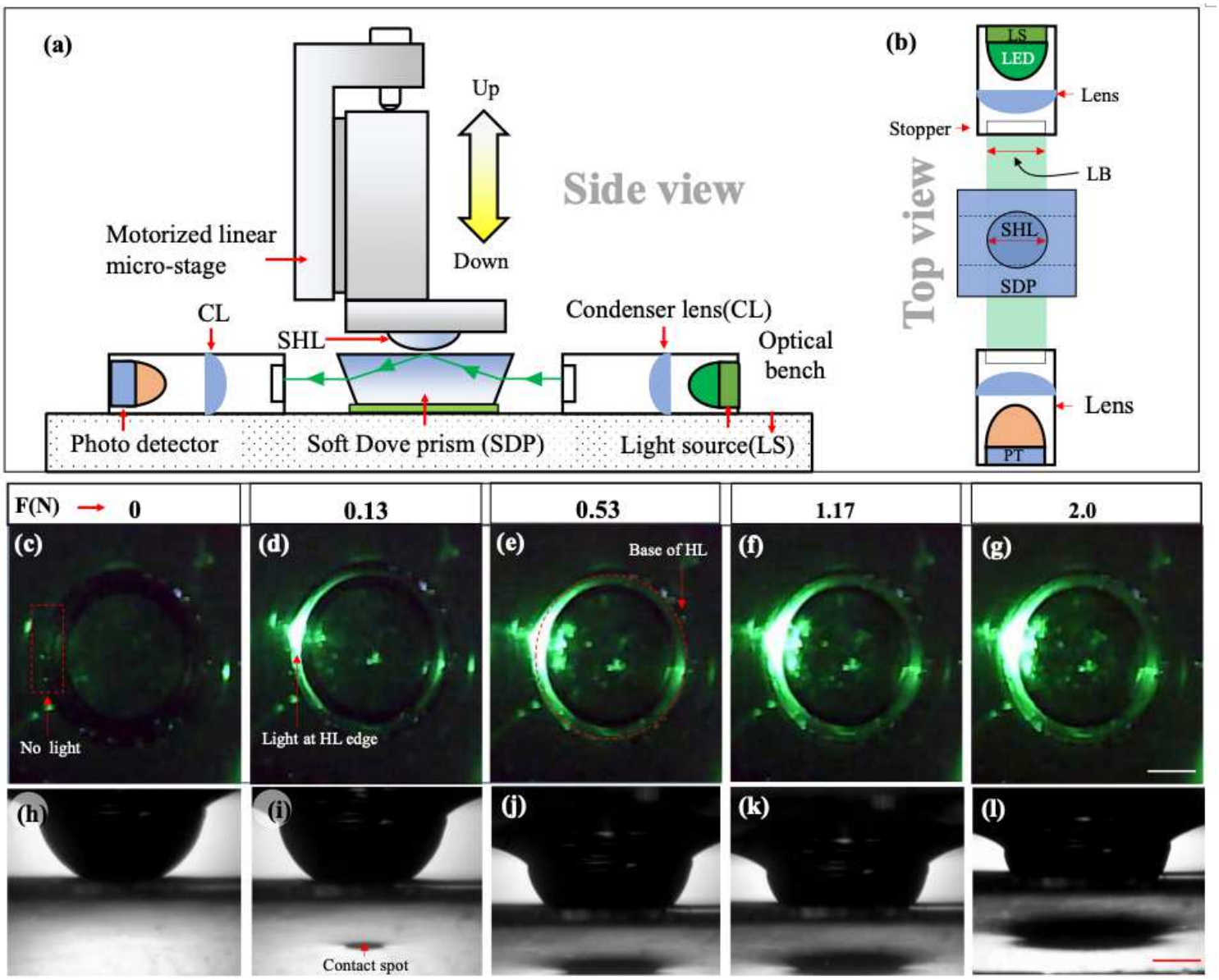

Figure 3

Characterization of the soft-a-skin. (a) Schematic diagram from the side view of a custom-made characterization tool for a soft-a-skin. (b) Top view of the of the experimental set up. (c-g) Images captured from top of the soft hemispherical lens (SHL) during the application of loads 0, 1.3, 0.53,1.17, and 2 N on the SHL. (h-l) Image captured from the side i.e. PT is replaced by camera and the images of both SHL and spot due to the load on SDP are captured.

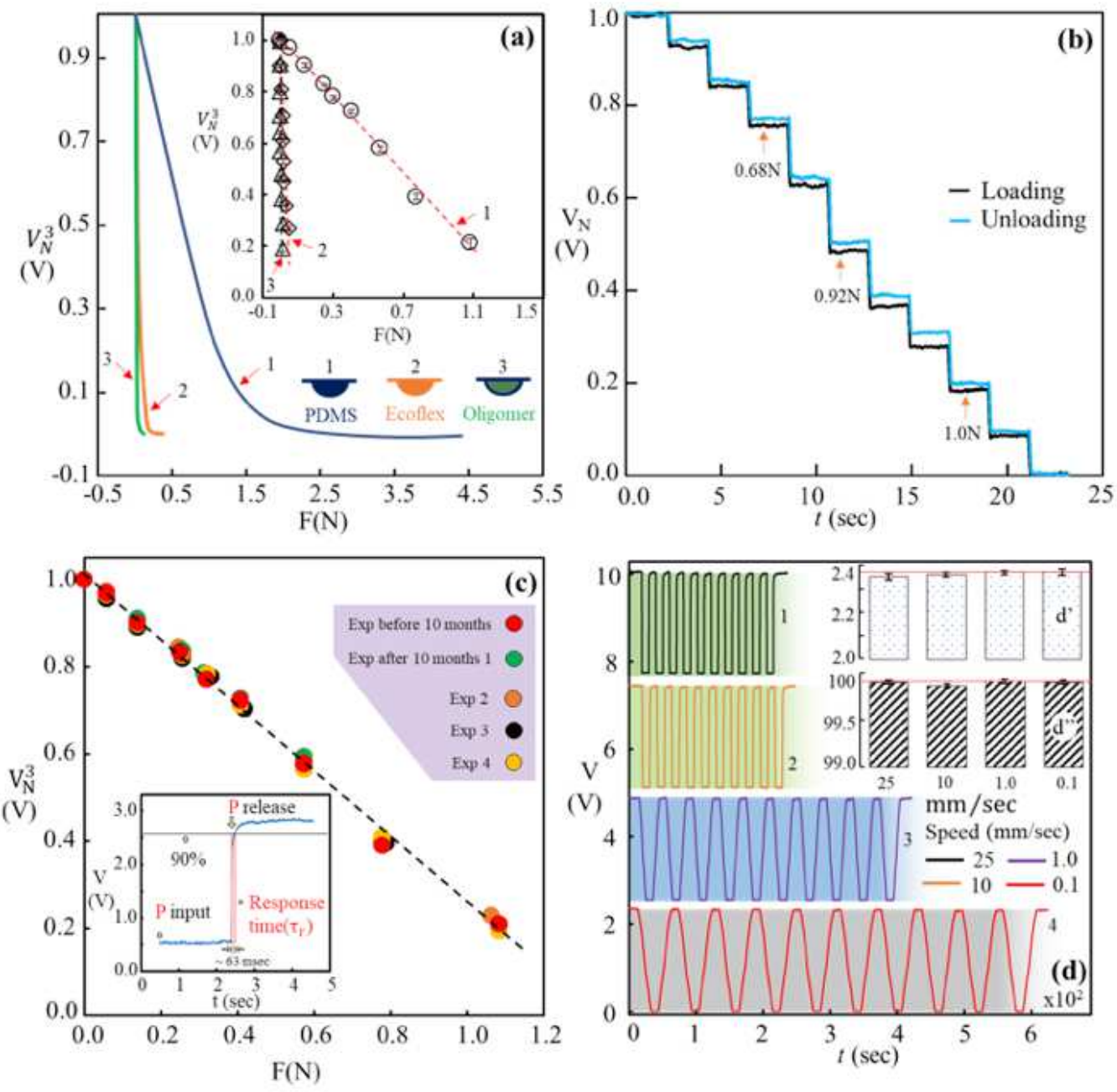

Figure 4

Characterization of the soft-a-skin unit node. (a) The plot shows the calibration between distance and load for various hemispherical lens of similar diameter 3mm. The curves 1, 2, and 3 depict SHL of 3 mm diameter made of PDMS, Ecoflex and PDMS membrane SHL filled with PDMS oligomer. (b) Step response in terms of normalized voltage at various applied loads and unloads. (c) Long term stability test in terms of soft-a-skin calibration and response time (insert image) (d) The repeatability and reproducibility of the sensor output with a wide range of speed of the soft hemispherical lens.

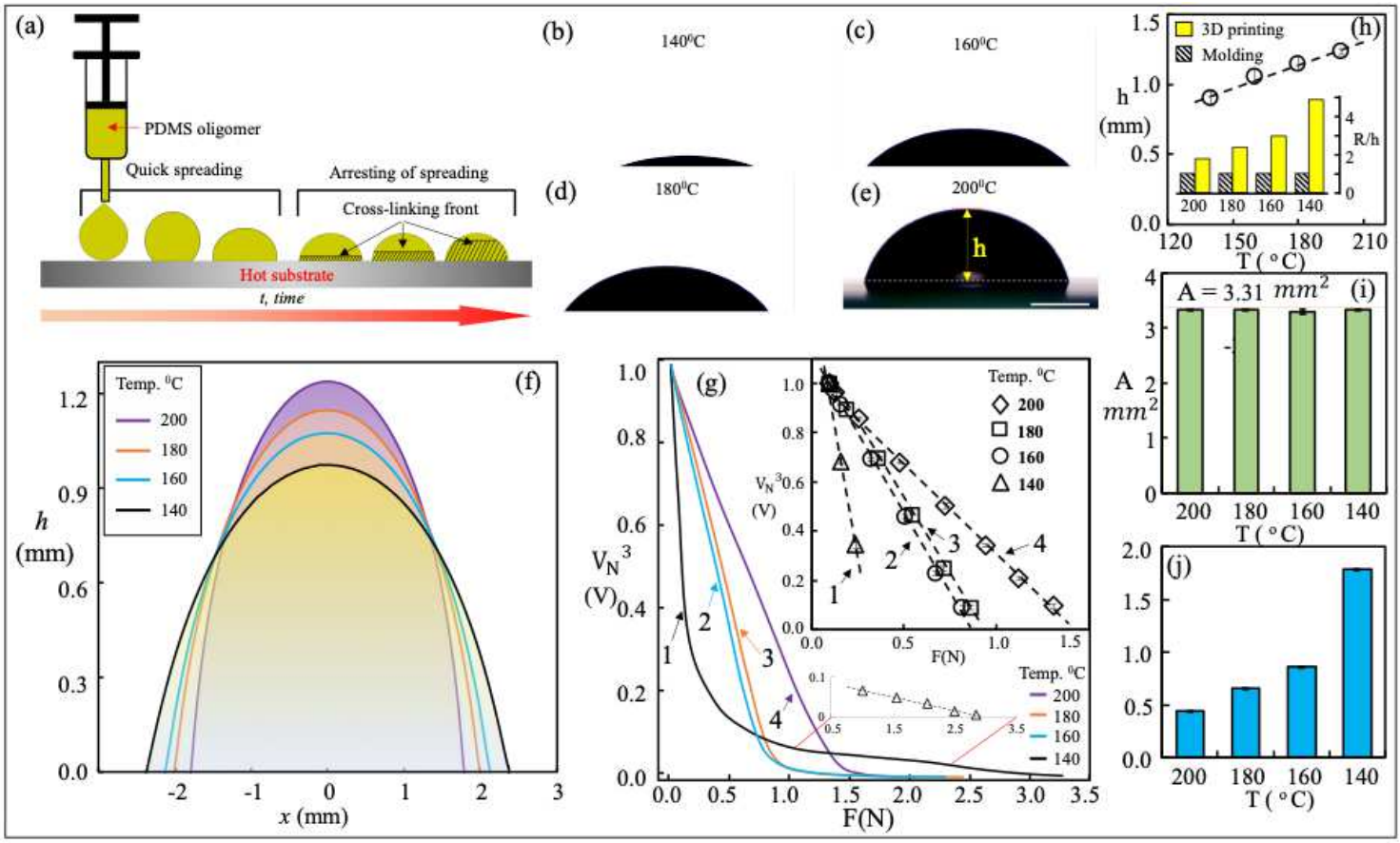

Figure 5

Characterization of 3D printable soft hemispherical lenses (SHL) on PDMS layer for making soft-a-skin. (a) Diagrammatic representation of rapid arresting of spreading of PDMS droplet due to thermal crosslinking. (b-e) Side view optical images of 3D printed lens on a thin sheet of PDMS layer at various film temperature. (f) Comparison of the surface profiles of the SHL at various film temperature (T_f). (g) The variation output intensity (V_N) at various applied load due to lenses fabricated using 3D printing at various T_f. (h) Dependence of the apex height (h) and the ratio of radius of curvature (R) to h of the lens with various T_f. (i) Bar chart of surface area of the lenses at various T_f (j) Bar chart shows variation of conic constant (k) a determining parameter of the shape of the curves due to various surface temperature.

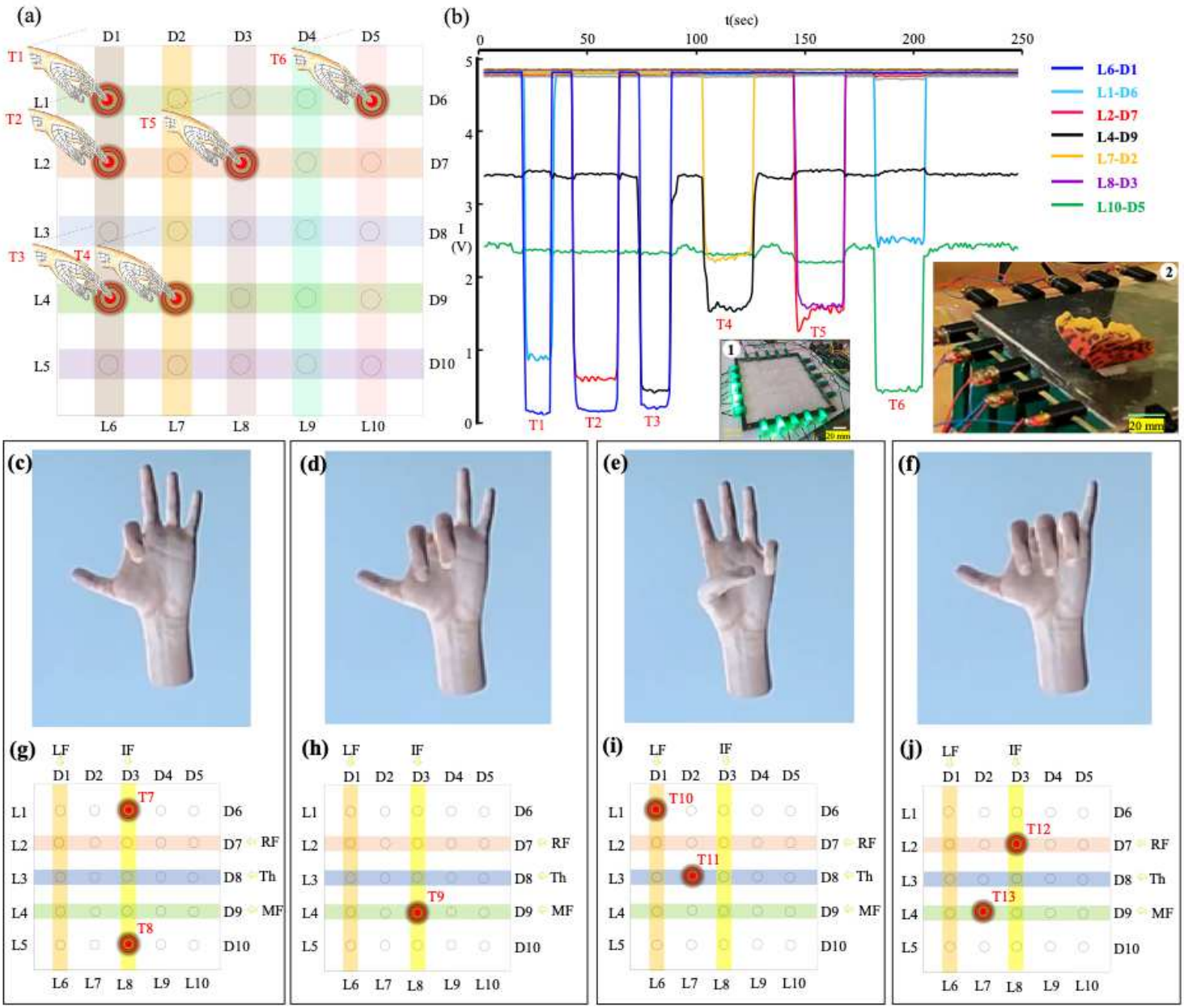

Figure 6

The visualization of the sensing capability of the soft-a-skin. (a) Diagrammatic representation of the soft-a-skin with the array of sensing nodes and their positions, light source, and the photo detectors. (b) Schematic representation of pressure perturbation created at the soft-a-skin node by a fingertip (see videos SI). (Fingers are connected to various sensors e.g., little finger (LF) to detector D1, ring finger (RF) to detector D7 and so on. Insert (b,1) optical image of a sensing node soft-a-skin made of PDMS SHLs and LEDs as light sources. Insert (b,2) demonstration of the PDMS soft-a-skin without SHLs and diodes LASERs as light sources and verify of the presence of butterfly on the soft-a-skin without SHLs. (c-f) Images of virtual hand posture result from the pressure exerted by the finger at various position represented as in the schematics(g-j) respectively.

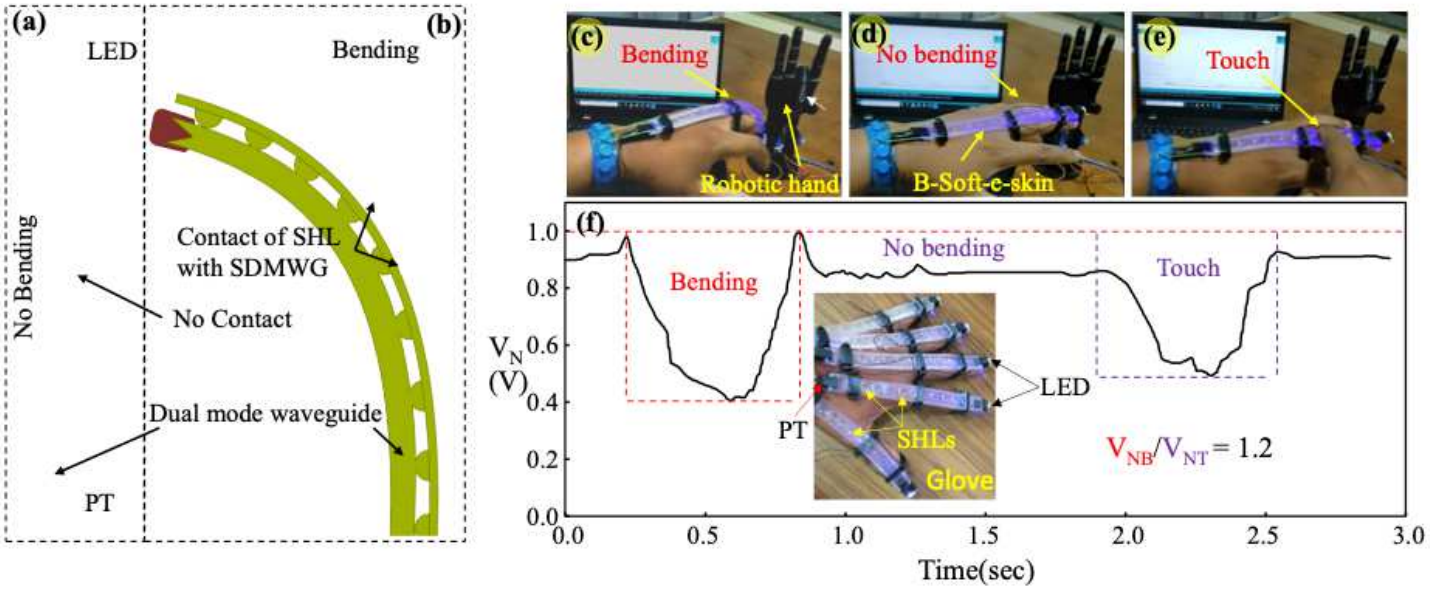

Figure 7

Bending with touch detection capability demonstration of the soft-a-skin(B-soft-a-skin). (a-b) Schematic diagram of B-soft-a-skin in normal position and bending positions respectively. (c-e) Images of finger flexing detection with the B-soft-a-skin, at bending, normal and with touch respectively. (f) B-soft-a-skin output signal for bending, normal and touch of the B-soft-a-skin. (see Video SV4)

Supplementary Files

This is a list of supplementary files associated with this preprint. Click to download.

- SoftaskinSI.docx
- SV1.mp4
- SV2.mp4
- SV3.mp4
- SV4.mp4